Journal of Information and Computing Science
J. Info. Comput. Sci., Vol. 18, No. 1, pp. 15-26

DOI: 10.4208/JICS-2023-002
June 2023

Analysis of blood through trapping vertical porous annulus with cilia in the presence of thermal radiation

Rizwan Ul Haq[1,*]

[1] *Department of Mathematics, School of Natural Sciences, National University of Science and Technology, Islamabad 44000, Pakistan*

Abstract. This study describes the analysis of nanofluid flow due to trapping along porous annulus with cilia in the presence of thermal radiation and heat absorption effects. In this examination, a partial differential equation is formulated to represent the two-dimensional movement of nanofluid. This system is developed in the cylindrical coordinates system and thereafter, a long wavelength approximation is introduced to attain the simplified form of the system. Emerging parameters are attained with nanoparticle's effects in the system. Effective thermal conductivity models for heat transfer analysis are utilized. Numerical solution has been calculated for pressure rise and pressure gradient. Velocity and temperature distribution is also plotted for physical parameters. It is important to find that the trend of velocity is increasing by improving the quantity of nanoparticle concentration, radiation and mixed convection parameters. By increasing the size of the radius, velocity profile and pressure gradient have decreasing trend.

AMS subject classifications: 65M22, 76D55, 80A20

Key words: Porous annulus, nanoparticles, heat absorption, thermal radiation, trapping arteries.

1 Introduction

Peristalsis stands as a significant mechanism responsible for the mixing and transportation of fluids. It emerges from the propagation of a sequential pattern of contraction and expansion along the inner surface of a tube. This intricate process facilitates the movement of fluids from regions of lower pressure to those of higher pressure, enabled by the

*Corresponding author. *Email addresses:* r.haq.qau@gmail.com (R. U. Haq)

advancing wave of contraction and expansion along the tube's pliable wall. This peristaltic mechanism serves various physiological functions, including transporting urine from the kidney to the bladder via the ureter, conveying chyme within the gastrointestinal tract, propelling spermatozoa through the ductus efferentes of the male reproductive tract, guiding the ovum along the fallopian tube, aiding in cilia transport, and maintaining blood circulation within narrow blood vessels. Moreover, peristaltic pumping finds practical application in numerous scenarios involving biomechanical systems. For specialized purposes, finger and roller pumps are commonly utilized to handle corrosive or exceptionally pure substances, ensuring that the fluid remains separate from the pump's internal surfaces. Additionally, leveraging the principles of peristalsis has led to the creation of various biomechanical instruments, such as the heart-lung machine.

Latham [1] was the first who made study for peristaltic flow. Later on Shapiro [2] explained this phenomenon in two dimensional flow. He considered the flow as inertia free with small wavelengths. Barton and Raynor [3] discussed peristaltic motion of two dimensional flow in tubes. They assumed a small Reynolds number. Shapiro et al. [4] talked about the peristaltic flow for both planar and axisymmetric cases. They applied the condition of long wavelength and very small Reynolds number. Yin and Fung [5] studied peristaltic pumping in the coordinate channel and axisymmetric tube. They assumed the condition of small wave length and low Reynolds number. Jaffrin [6] examined the inertia and streamline curvature impact on peristaltic flow. Jaffrin and Shapiro [7] represented peristaltic flow in distinctive routines. They studied peristaltic motion in the presence of pressure gradients. For circular cylindrical tubes peristaltic pumping is deliberated by Takabatake et al [8]. In another study Mekhiemer [9] examined the peristaltic movement of couple stress within a ring-shaped region using an endoscope.

Cilia are microscopic hair-like structures found in the respiratory, digestive, and reproductive systems of both males and females, as well as in the nervous system across various animal species. They hold significant functions in processes such as movement, locomotion, feeding, circulation, breathing, and reproduction. Cilia primarily serve to transport fluids, utilizing their synchronized beating to create a metachronal wave. This wave-like motion, resulting from the coordinated movement of cilia, is facilitated by the flexible envelope of cilia tips. This envelope, forming the metachronal wave, acts as a stretchable barrier, consistently propelling forward motion in a singular direction.

Agrawal and Anawaruddin [10] talked about cilia transference of biofluid with variable thickness. Barton and Raynor [11] discussed mucus flow due to motion of cilia. [12, 13] analysed hydrodynamics of protozoa that they utilize cilia for movement. Vélez-Cordero and Lauga [14] explained the envelope model of cilia by taking Newtonian fluid. Mechanical features of cilia were presented by Rydholm et al. [15]. Basten and Giles [16] discussed function of cilia. Nadeem and Sadaf [17] analyzed the ciliary motion in annulus with nanofluid. Nonetheless, the exploration of ciliary motion within a porous medium containing nanofluid remains largely uncharted. Consequently, the primary aim of this research is to delve into the theoretical examination of nanofluid behavior within a porous annulus, driven by a metachronal wave of cilia, while also accounting

for the influence of thermal radiation.

In the recent years, various researchers has been working in the field of blood flow through trapping annulus. Recently, Javaria et al. [18] analysed the blood based graphene oxide nanofluid that passes through capillary with electromagnetic field. In the similar manner, Devakar et al. [19] has investigated the peristaltic propulsion of couple stress fluid flow in a tube having the endoscope. On the basis of MHD effects, results are determined for the fluid flow and heat transfer. It is found in the literature that MHD resist the fluid flow and pumping rate of peristaltic flow and it rise the within the tube. Asghar et al. [20] presented a detail study for various nanoparticle in a micro-vessel. This study reports the simulation of hemodynamic effects of bloodstream for ternary hybrid nanofluid model. In the recent years, Yadav et al. [21] presented the flow in a porous region between coaxial deformable tubes.

Based upon the above mentioned studies, we have developed our problem for vertically annulus that is filled through blood base nanoparticles. Furthermore, thermal radiation effects are also considered by using Rosland approximation. The mathematical model is entirely constructed by the partial differential equations and then by using the long wavelength approximations, it is simplified into a couple ordinary equations. A numerical technique is applied to handle the annulus problem and obtain the stable results that must satisfy the boundary condition according to the described mathematical model. Emerging parameters are raised along with the effects of nanoparticles in the complete model. These parameters have significant effects on each flow behaviour and heat transfer. It is further described how the radius of the inner cylinder affects the molecules of the blood which are enclosed in the annulus.

2 Formulation of model

Consider the cilia motion of 2-D incompressible flow of nanofluid within a porous annular region under the influence of thermal radiation. Continuity and momentum equations can be formulated as [17].

$$\frac{\partial \tilde{U}}{\partial \tilde{R}} + \frac{\tilde{U}}{\tilde{R}} + \frac{\partial \tilde{w}}{\partial \tilde{Z}} = 0 \tag{2.1}$$

$$\rho_{nf}\left(\frac{\partial \hat{U}}{\partial \hat{t}} + \hat{U}\frac{\partial \hat{U}}{\partial \hat{R}} + \hat{W}\frac{\partial \hat{U}}{\partial \hat{Z}}\right) = -\frac{\partial \hat{P}}{\partial \hat{R}} + \mu_{nf}\left(\frac{1}{\tilde{R}}\frac{\partial}{\partial \tilde{R}}\left(\tilde{R}\frac{\partial \tilde{U}}{\partial \tilde{R}}\right) - \frac{\tilde{U}}{\tilde{R}^2} + \frac{\partial^2 \tilde{U}}{\partial \tilde{Z}^2}\right) \tag{2.2}$$

$$\begin{aligned}\rho_{nf}\left(\frac{\partial \hat{W}}{\partial \hat{t}} + \hat{U}\frac{\partial \hat{W}}{\partial \hat{R}} + \hat{W}\frac{\partial \hat{W}}{\partial \hat{Z}}\right) = &-\frac{\partial \hat{P}}{\partial \hat{Z}} + \mu_{nf}\left(\frac{1}{\hat{R}}\frac{\partial}{\partial \hat{R}}(\hat{R}\frac{\partial \hat{W}}{\partial \tilde{R}}\right) - \frac{\mu_{nf}}{k_0}\hat{W} + \frac{\partial^2 \hat{W}}{\partial \hat{Z}^2}) \\ &+ (\rho\beta)_{nf}\ \hat{g}\ (\hat{T} - \hat{T}_1)\end{aligned} \tag{2.3}$$

$$(\rho c_p)_{nf}\left(\frac{\partial \hat{T}}{\partial \hat{t}} + \hat{U}\frac{\partial \hat{T}}{\partial \hat{R}} + \hat{W}\frac{\partial \hat{T}}{\partial \hat{Z}}\right) = k_{nf}\left(\frac{\partial^2 \hat{T}}{\partial \hat{R}^2} + \frac{1}{\hat{R}}\frac{\partial \hat{T}}{\partial \hat{R}} + \frac{\partial^2 \tilde{T}}{\partial \hat{Z}^2}\right) + \frac{\mu_{nf}}{k_0}\hat{W}^2 - \frac{\partial q_r}{\partial \hat{R}} + Q_0 \tag{2.4}$$

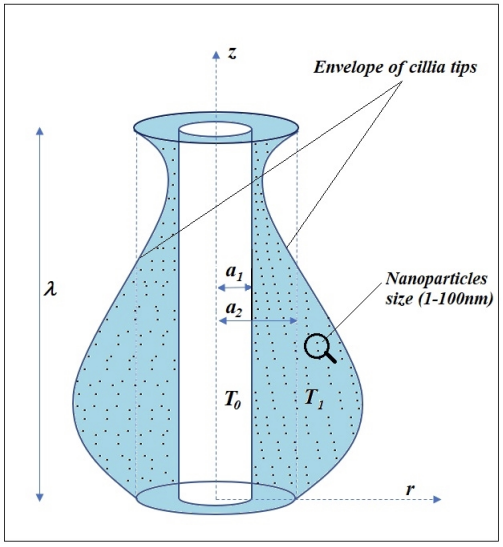

Figure 1: Geometry of the model.

Table 1: Thermo physical properties of nanoparticles and fluid

Physical properties	Copper	Pure blood
$c_p(\frac{J}{kgK})$	385	3594
$\rho(\frac{kg}{m^3})$	8933	1063
$k(\frac{W}{mk})$	400	0.492
$\beta.10^{-5}(\frac{1}{K})$	1.67	0.18

The radiative heat flux is

$$q_r = \frac{16\sigma^* {T_0}^3}{3k^*}\frac{\partial T}{\partial \tilde{R}}.$$

Heat capacity and thermal conductivity of nanofluid express as follows [22,23]

$$\alpha_{nf} = \frac{k_{nf}}{(\rho c_p)_{nf}} \qquad \mu_{nf} = \frac{\mu_f}{(1-\phi)_{2.5}} \quad \rho_{nf} = (1-\phi)\rho_f + \phi\rho_s$$

$$(\rho\beta)_{nf} = (1-\phi)\rho_f\beta_f + \phi\rho_s\beta_s \quad (\rho c_p)_{nf} = (1-\phi)(\rho c_p)_f + \phi(\rho c_p)_s \tag{2.5}$$

$$\frac{k_{nf}}{k_f} = \frac{(k_s+2k_f)-2\phi(k_f-k_s)}{(k_s+2k_f)+\phi(k_f-k_s)}$$

Based on the depicted metachronal wave shape in Figure 1, it is posited that the mathematical expression for the envelope of cilia tips can be described as follows.

$$\hat{R} = \hat{g}(\hat{Z}, \hat{t}) = \left[a_2 + a_2\epsilon\cos\left(\frac{2\pi}{\lambda}(\hat{Z} - c\hat{t})\right)\right] = \hat{R}_2. \tag{2.6}$$

In the light of various examples of cilia movement analysed by Sleigh [24], vertical side of cilia's tip which are expressed through the expression:

$$\hat{Z}=\hat{h}(\hat{Z},\hat{Z}_0,\hat{t})=\hat{Z}_0+a_2\alpha\epsilon sin\big(\frac{2\,\pi}{\lambda}(\hat{Z}-c\hat{t})\big). \tag{2.7}$$

When the no-slip condition is enforced at the channel walls, the velocities transferred to the fluid particles align with those of the cilia tips. The vertical and horizontal velocities of the cilia are as follows.

$$\begin{aligned}\hat{W}&=\frac{\partial\hat{Z}}{\partial\hat{t}}=\frac{\partial\hat{h}}{\partial\hat{t}}+\frac{\partial\hat{h}}{\partial\hat{Z}}\,\frac{\partial\hat{Z}}{\partial\hat{t}}=\frac{\partial\hat{h}}{\partial\hat{t}}+\frac{\partial\hat{h}}{\partial\hat{Z}}\hat{W},\\ \hat{U}&=\frac{\partial\hat{R}}{\partial\hat{t}}=\frac{\partial\hat{g}}{\partial\hat{t}}+\frac{\partial\hat{g}}{\partial\hat{Z}}\,\frac{\partial\hat{Z}}{\partial\hat{t}}=\frac{\partial\hat{g}}{\partial\hat{t}}+\frac{\partial\hat{f}}{\partial\hat{Z}}\hat{W}\end{aligned} \tag{2.8}$$

Solving (2.6)−(2.8), we get

$$\begin{cases}\hat{W}=\hat{\chi}(\hat{Z},\hat{t})=\dfrac{\frac{-2\pi}{\lambda}a_2c\epsilon\alpha\cos\big(\frac{2\pi}{\lambda}(\hat{Z}-c\hat{t})\big)}{1-\frac{2\pi}{\lambda}a_2\epsilon\alpha\cos\big(\frac{2\pi}{\lambda}(\hat{Z}-c\hat{t})\big)}\\ \hat{U}=\dfrac{\frac{2\pi}{\lambda}a_2c\epsilon\sin\big(\frac{2\pi}{\lambda}(\hat{Z}-c\hat{t})\big)}{1-\frac{2\pi}{\lambda}a_2\epsilon\alpha\cos\big(\frac{2\pi}{\lambda}(\hat{Z}-c\hat{t})\big)} \quad \text{at} \quad \hat{R}=\hat{R}_2.\end{cases} \tag{2.9}$$

Following transformations are used

$$r=\hat{R},\;\; \hat{z}=\hat{Z}-c\hat{t},\;\; \hat{u}=\hat{U},\hat{w}=\hat{W}-c. \tag{2.10}$$

Suitable boundary conditions are formulated as

$$\begin{aligned}&\hat{W}=0 \quad at \quad \hat{R}=\hat{R}_1\\ &\hat{W}=\hat{\chi}(\hat{Z},\hat{t}) \quad at \quad \hat{R}=\hat{R}_2=\; a_2+a_2\epsilon\cos(\frac{2\pi}{\lambda}(\hat{Z}-c\hat{t})).\end{aligned} \tag{2.11}$$

Non dimensional variables are defined as:

$$\begin{aligned}&R=\frac{\hat{R}}{a_2},\; p=\frac{a_2^2\hat{p}}{c\lambda\mu_f},\; r=\frac{\hat{r}}{a_2},\; \delta=\frac{a_2}{\lambda},\; Z=\frac{\hat{Z}}{\lambda},\; t=\frac{c\hat{t}}{\lambda},\; Re=\frac{ac\rho_f}{\mu_f},\\ &u=\frac{\lambda\hat{u}}{a_2c},\; W=\frac{\hat{W}}{c},\; w=\frac{\hat{w}}{c},\; r_1=\frac{\hat{r}_1}{a_2}=\frac{a_1}{a_2}=\xi,\; \theta=\frac{\hat{T}-\hat{T}_1}{\hat{T}_0-\hat{T}_1},\; U=\frac{\lambda\hat{U}}{a_2c},\\ &B=\frac{Q_0a^2}{k_f(\hat{T}_0-\hat{T}_1)},\; G_r=\frac{g\;\beta_f\;\rho_f\;a^2(\hat{T}_0-\hat{T}_1)}{c\mu_f},\; r_2=\frac{\hat{r}_2}{a_2}=1+\epsilon\;\cos(2\pi z).\end{aligned} \tag{2.12}$$

After using dimensionless parameters, applying the conditions of low Reynolds number, long wave length approximation and transformation defined in (2.10) and (2.12), (2.2)−(2.4) becomes

$$\frac{\partial\,p}{\partial\,r}=\;0, \tag{2.13}$$

$$-\frac{\partial p}{\partial z}+\frac{\mu_{nf}}{\mu_f}\left[\frac{1}{r}\frac{\partial}{\partial r}\left(r\frac{\partial w}{\partial r}\right)-(w+1)\sigma^2\right]+\frac{(\rho\beta)_{nf}}{(\rho\beta)_f}G_r\theta=0, \tag{2.14}$$

$$\frac{\alpha_{nf}}{\alpha_f}\left[\frac{1}{r}\frac{\partial\theta}{\partial r}+(1+Rn)\frac{\partial^2\theta}{\partial r^2}+\sigma^2E_m(w+1)^2\right]+B\frac{(\rho c_p)_f}{(\rho c_p)_{nf}}=0, \tag{2.15}$$

where

$$\sigma^2=\frac{{a_2}^2}{k_0},E_m=\frac{c^2\mu_{nf}}{k_{nf}(\tilde{T}_0-\tilde{T}_1)},Rn=\frac{16\sigma^*{T_0}^3}{3k^*}\frac{\sigma_f}{k_{nf}},\sigma_f=\frac{a_2^2}{(\tilde{T}_0-\tilde{T}_1)}.$$

Boundary conditions after dimensionless parameters are

$$w=-1-2\pi\epsilon\alpha\delta\cos(2\pi z)\quad at\quad r=r_2, \tag{2.16}$$

$$w=-1\quad at\quad r=r_1, \tag{2.17}$$

$$\theta\ =\ 1\quad at\quad r=r_1\ ,\theta=\ 0\quad at\quad r=r_2, \tag{2.18}$$

$$u\ =2\pi\epsilon\sin(2\pi z)+(2\pi)^2\epsilon\alpha\delta\cos(2\pi z)\sin(2\pi z)\quad at\quad r=\ r_2. \tag{2.19}$$

3 Methodology and Graphical results

In the current mathematical model, we have found the numerical solution. For numerical simulations, builtin NDsolve numerical scheme is used to find the numerical solution. Table 1 described the numerical values of thermophysical properties of nanofluid. For numerical validation, we have found the numerical tables 2−4 against the velocity profiles for various values of emerging parameters.

Table 2: Velocity profile for $w(r)$ at $r_1=0.1$, $\sigma=0.1$, $Em=0.1$, $z=0.08$, $\Phi=0.02$, $\epsilon=0.05$, $Rn=1$, $B=0.17$, $\delta=0.11$, $\alpha=0.02$

r	$G_r=1$	$G_r=2$	$G_r=3$	$G_r=4$
0.1	-1	-1	-1	-1
0.2	-0.958843	-0.917463	-0.876083	-0.834703
0.3	-0.946129	-0.891910	-0.837691	-0.783472
0.4	-0.946314	-0.892196	-0.838078	-0.783960
0.5	-0.953436	-0.906381	-0.859325	-0.812270
0.6	-0.964075	-0.927616	-0.891157	-0.854697
0.7	-0.975826	-0.951087	-0.926347	-0.901608
0.8	-0.986787	-0.972988	-0.959189	-0.945391
0.9	-0.995347	-0.990096	-0.984844	-0.979592
1	-1.000080	-0.999550	-0.999022	-0.998494

This section thoroughly explains the analysis of results constructed for velocity, temperature, pressure gradient. These results are sketched through graphs in Figures 2−6

Table 3: Velocity profile for $w(r)$ at $r_1=0.1$, $\sigma=0.1$, $G_r=3$, $Em=0.1$, $z=0.08$, $\epsilon=0.05$, $Rn=1$, $B=0.17$, $\delta=0.11$, $\alpha=0.02$

r	$\phi=0.01$	$\phi=0.02$	$\phi=0.03$	$\phi=0.04$
0.1	-1	-1	-1	-1
0.2	-0.911467	-0.876083	-0.842582	-0.81092
0.3	-0.884048	-0.837691	-0.793808	-0.752338
0.4	-0.884341	-0.838078	-0.794249	-0.752913
0.5	-0.899544	-0..859325	-0.821262	-0.785300
0.6	-0.922314	-0.891157	-0.861673	-0.833822
0.7	-0.947485	-0.926347	-0.906348	-0.887458
0.8	-0.970978	-0.959189	-0.948038	-0.937506
0.9	-0.989330	-0.984844	-0.980601	-0.976595
1	-0.999473	-0.999022	-0.998596	-0.998193

show the behaviour of axial velocity for ϕ (nanoparticle concentration that ranges from 0-0.06), G_r (Grashof number that ranges from 1-7), σ (porosity parameter that ranges from 1-7), Rn (radiation parameter that ranges from 0.1-0.7), r_1 (ratio of the radius of tubest hat ranges from 0.1-0.7). The numerical tables (see Tables 2 and 3) are also presented to describe the behaviour of velocity against the above said parameters. Similarly, Table 4 described the behavior of temperature profile at various position of radius.

Table 4: Temperature profile for $\theta(r)$ at $r_1=0.1$, $\sigma=0.1$, $G_r=1$, $Em=0.5$, $z=0.03$, $\epsilon=0.05$, $Rn=1$, $B=6$, $\delta=0.11$ $\alpha=0.02$

r	$\phi=0.02$	$\phi=0.04$	$\phi=0.06$	$\phi=0.08$
0.1	1	1	1	1
0.2	0.976894	0.967749	0.959255	0.951346
0.3	0.933736	0.919010	0.905333	0.892596
0.4	0.871104	0.853156	0.836486	0.820962
0.5	0.789224	0.769945	0.752040	0.735365
0.6	0.688211	0.669254	0.651647	0.635250
0.7	0.568133	0.551008	0.535101	0.520289
0.8	0.429036	0.415159	0.402270	0.390267
0.9	0.270950	0.261674	0.253059	0.245036
1	0.093897	0.090529	0.087400	0.084487

Figures 2 and 3 represent the effects of ϕ (nanoparticle concentration) and G_r (Grashof number) over velocity profile $w(r,z)$. It is depicted that with the increase in ϕ and G_r , velocity profile increases. Figure 4 shows decrease in velocity when σ (porosity parameter) is increased. Effect of Rn (radiation parameter on axial velocity w is analyzed through Figure 5. Velocity increases with an increase in Rn. The variation in velocity profile due

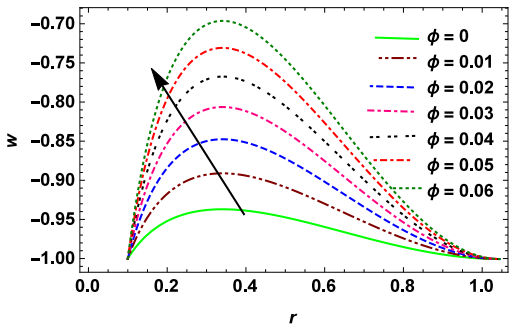

Figure 2: Velocity profile for fixed parameter are α=0.02, δ=0.11, B=0.17, G_r=3, z=0.08, Rn=1, ϵ=0.05, E_m=0.1, σ=0.1 ξ=0.18

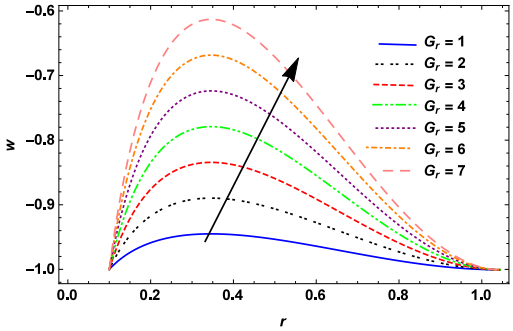

Figure 3: Velocity profile for fixed parameter are α=0.02, δ=0.11, B=0.17, ϕ=0.02, z=0.08, Rn=1, ϵ=0.05, E_m=0.1, σ=0.1,ξ=0.18

to change in radius of tubes is illustrated in Figure 6. Here velocity is decreasing function of r_1.

Temperature profile $\theta(r,z)$ is plotted against the radial axis r in Figures 7−9 for different values of ϕ (solid volume fraction of the nanoparticle), B (Heat source parameter) and Rn (radiation parameter). Figure 7 illustrates the impact of B (Heat source parameter) on temperature. Here, increasing behaviour of θ is noted for larger values of B. As illustrated in Figure 8, it becomes evident that an augmentation in nanoparticle concentration leads to a reduction in fluid temperature. This phenomenon can be attributed to the substantial thermal conductivity of the nanofluid, which facilitates rapid dissipation. This observation rationalizes the utilization of copper nanoparticles, in various forms, as an efficient coolant. Figure 9 elucidates the impact of Rn (radiation parameter) on θ. It can be seen that temperature decreases for increasing values of Rn.

Graphs for pressure gradient are shown in Figures 10−12. The graphs indicate that pressure gradient is inversely proportional to σ (porosity of parameter) and ϕ (solid volume fraction of the nanoparticle) but it is directly proportional to ϵ (cilia length). From Figures 10−11, it is observed that with increase in ϕ and σ, pressure gradient decreases. Figure 12 illustrates that pressure gradient increases with increase in cilia length. The pressure rise Δp against the flow rate Q is plotted for various variations of physical parameters in Figures 13−15. It is perceived from Figures 13 and 14 that pressure rise increases in the region Q $\in [-1, 0]$ and on the other hand it decreases in the domain Q $\in [0, 1]$. It is clear from Figure 15 that increase in cilia length pressure rise increases in region Q $\in [-1, 0.1]$ and reduces in Q $\in [0.1, 1]$.

4 Conclusions

In the present study, we have considered the results of nanofluid due to cilia motion in the porous annulus in the presence of thermal radiation. Major findings are described as follows.

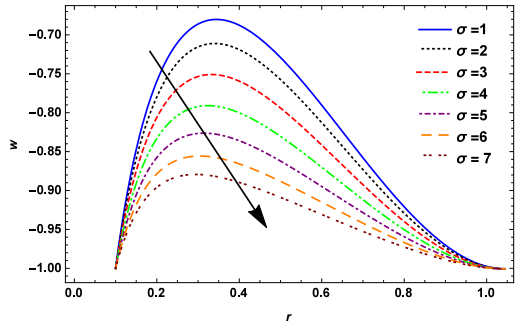

Figure 4: Velocity profile for fixed parameter are α=0.02, δ=0.11, B=0.17, ϕ=0.02, z=0.08, Rn=1, ϵ=0.05, E_m=0.1, G_r=6,ξ=0.18

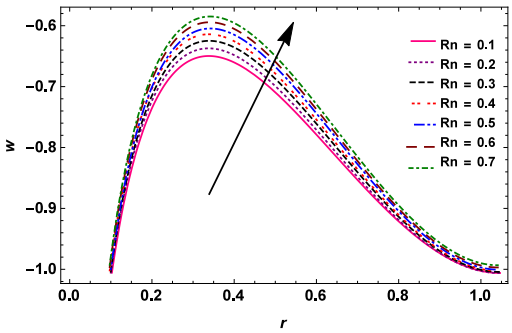

Figure 5: Velocity profile for fixed parameter are α=0.02, δ=0.11, B=0.17, ϕ=0.04, z=0.08, G_r=5, ϵ=0.05, E_m=0.1, σ=0.1,ξ=0.18

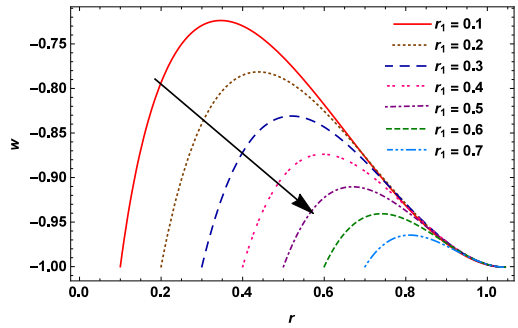

Figure 6: Velocity profile for fixed parameter are α=0.02, δ=0.11, B=0.17, ϕ=0.02, z=0.08, Rn=1, ϵ=0.05, E_m=0.1, σ=0.1, G_r=5

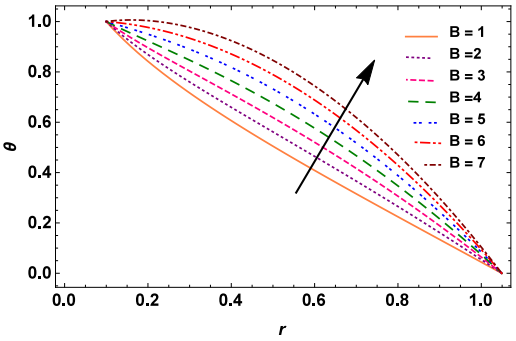

Figure 7: Temperature profile for fixed parameter are α=0.02, δ=0.11, Φ=0.02, ξ=0.1, z=0.03, Rn=1, ϵ=0.05, E_m=0.5, σ=0.1, G_r=1

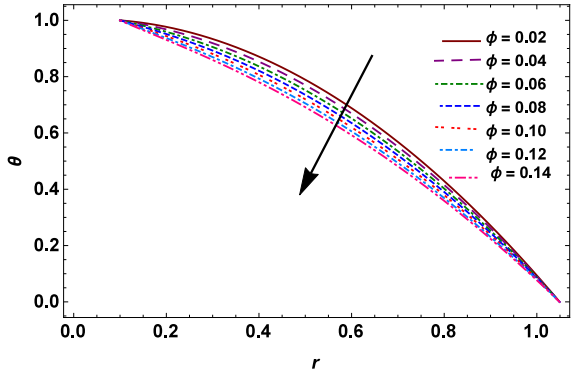

Figure 8: Temperature profile for fixed parameter are α=0.02, δ=0.11, ξ=0.1, z=0.03, Rn=1, ϵ=0.05, E_m=0.5, σ=0.1, G_r=1, B=6

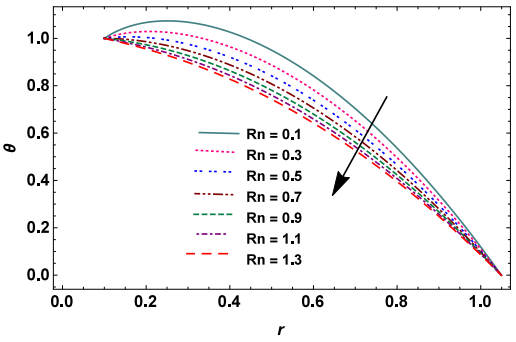

Figure 9: Temperature profile for fixed parameter are α=0.02, δ=0.11, ξ=0.1, z=0.03, ϕ=0.04, ϵ=0.05, E_m=0.5, σ=0.1, G_r=1, B=4

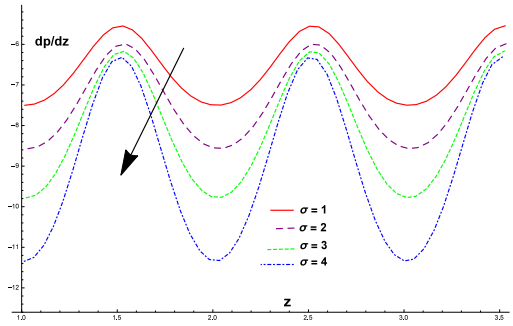

Figure 10: Pressure gradient for fixed parameter are $\alpha=0.02$, $\xi=0.1$, $\delta=0.11$, $\phi=0.02$, $\epsilon=0.05$

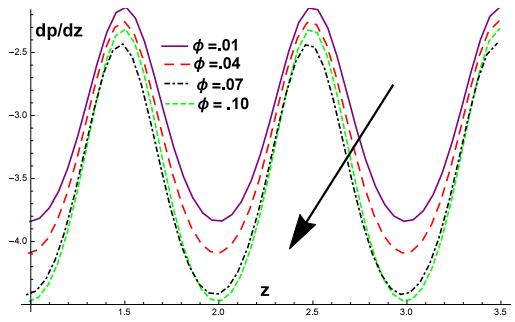

Figure 11: Pressure gradient for fixed parameter are $\alpha=0.02$, $\xi=0.1$, $\delta=0.11$, $\sigma=0.01$, $\epsilon=0.05$

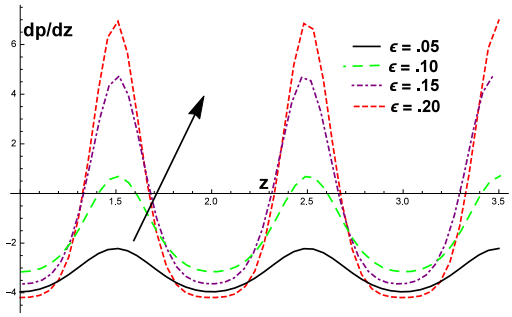

Figure 12: Pressure gradient for fixed parameter are $\alpha=0.02$, $\xi=0.1$, $\delta=0.11$, $\phi=0.02$, $\sigma=0.01$

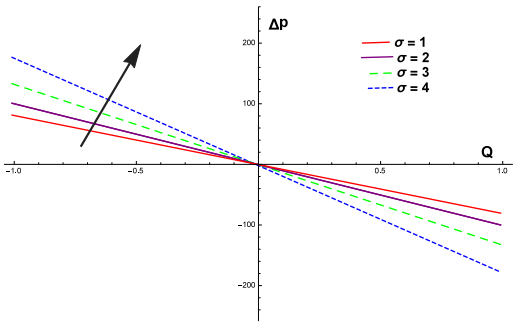

Figure 13: Pressure rise for fixed parameter are $\alpha=0.02$, $\xi=0.1$, $\delta=0.11$, $\phi=0.02$, $\epsilon=0.05$

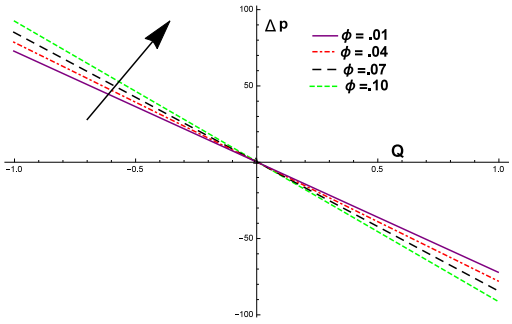

Figure 14: Pressure rise for fixed parameter are $\alpha=0.02$, $\xi=0.1$, $\delta=0.11$, $\sigma=0.01$, $\epsilon=0.05$

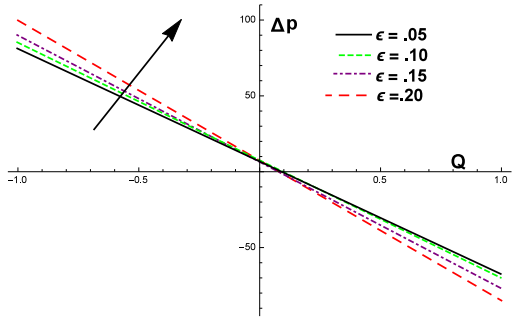

Figure 15: Pressure rise for fixed parameter are $\alpha=0.02$, $\xi=0.1$, $\delta=0.11$, $\sigma=0.01$, $\epsilon=0.05$

- Velocity field increases due to the increase in ϕ, G_r.
- Velocity is inversely proportional to the porosity parameter.
- Temperature of fluid is declining when nanoparticles and thermal radiation is added to base fluid.
- Temperature of fluid is increasing with respect to increasing values of heat source parameter.
- Pressure gradient reduces for rising values of both ϕ and σ.
- Pressure gradient rises when the length of cilia is extended.
- Pressure rise increases in the negative domain but decreases in the positive domain of flow rate.

Conflicts of Interest

The authors declare no conflict of interest.

References

[1] T. W. Latham, *Fluid motion in a peristaltic pump*, Master's thesis, Massachusetts Institute of Technology, Cambridge, 1966.
[2] A. H. Shapiro, Pumping and retrograde diffusion in peristaltic wave, In *Proceedings Workshop on Ureteral Reflux in Children*, Washington DC, 1967, National Academy of Sciences.
[3] C. Barton and S. Raynor, Peristaltic flow in tubes, *Bull. Math. Biophys.*, 1968, 30: 663–680.
[4] A. H. Shapiro, M. Y. Jaffrin, and S. L. Weinberg, Peristaltic pumping with long wave length at low reynolds numbers, *J. Fluid Mech.*, 1969, 37: 799–825.
[5] F. Yin and Y. C. Fung, Peristaltic wave in circular cylindrical tubes, *J. Appl. Mech.*, 1969, 36: 579–587.
[6] M. Y. Jaffrin, Inertia and streamline curvature effects in peristaltic pumping, *Int. J. Eng. Sci.*, 1973, 11: 681–699.
[7] M. Y. Jaffrin and A. H. Shapiro, Peristaltic pumping, *Annu. Rev. Fluid Mech.*, 1971, 3: 13–37.
[8] S. Takabatake, K. Ayukawa, and A. Mpri, Peristaltic pumping in circular tubes: a numerical study of fluid transport and its efficiency, *J. Fluid Mech.*, 1988, 193: 267–283.
[9] K. S. Mekheimer and Y. A. Elmaboud, Peristaltic flow of a couple stress fluid in an annulus: Application of an endoscope, *Phys. A*, 2008, 387(11): 2403–2415.
[10] H. L. Agrawal and Anawaruddin, Cilia transport of bio fluid with variable viscosity, *Indian J. Pure Appl. Math.*, 1984, 15: 1128–1139.
[11] C. Barton and S. Raynor, Analytical investigation of cilia induced mucus flow, *Bull. Math. Biophy.*, 1967, 29: 419–428.
[12] T. L. Jahn and E. C. Bovee, Movement and locomotion of microorganisms, *Annu. Rev. Microbiol.*, 1965, 19: 21–58.

[13] T. L. Jahn and E. C. Bovee, Motile behaviour of protozoa, In *Research in Protozoology*, volume 140, 1967.
[14] J. R. Vélez-Cordero and E. Lauga, Waving transport and propulsion in a generalized newtonian fluid, *J. Non-Newtonian Fluid Mech.*, 2013, 199: 37–50.
[15] S. Rydholm et al., Mechanical properties of primary cilia regulate the response of fluid flow, *Am. J. Physiol., Renal Physiol.*, 2010, 298(5): F1096–F1102.
[16] S. G. Basten and R. H. Giles, Functional aspects of primary cilia in signaling, cell cycle and tumorigenesis, *Cilia*, 2013, 2(1): 6.
[17] S. Nadeem and H. Sadaf, Trapping study of nanofluids in an annulus with cilia, *AIP Adv.*, 2015, 5(12): 127204.
[18] J. Akram, N. S. Akbar, and D. Tripathi, Blood-based graphene oxide nanofluid flow through capillary in the presence of electromagnetic fields: A sutterby fluid model, *Microvasc. Res.*, 2020, 132: 104062.
[19] M. Devakar, K. Ramesh, and K. Vajravelu, Magnetohydrodynamic effects on the peristaltic flow of couple stress fluid in an inclined tube with endoscope, *J. Comput. Math. Data Sci.*, 2022, 2: 100025.
[20] A. Ali, S. Das, and T. Muhammad, Dynamics of blood conveying copper, gold, and titania nanoparticles through the diverging/converging ciliary micro-vessel: Further analysis of ternary-hybrid nanofluid, *J. Mol. Liq.*, 2023, 390(Part A): 122959.
[21] P. K. Yadav and M. Roshan, Mathematical modeling of blood flow in an annulus porous region between two coaxial deformable tubes: An advancement to peristaltic endoscope, *Chin. J. Phys.*, 2024, 88: 89–109.
[22] N. S. Akbar and A. W. Butt, Cnt suspended nanofluid analysis in a flexible tube with ciliated walls, *Eur. Phys. J. Plus*, 1989, 129: 174.
[23] M. H. M. Yasin, N. M. Arifin, R. Nazar, F. Ismail, and I. Pop, Mixed convection boundary layer flow embedded in a thermally stratified porous medium saturated by a nanofluid, *Adv. Mech. Eng.*, 2013, 5: 121943.
[24] M. A. Sleigh, Patterns of ciliary beating, *Symp. Soc. Exp. Biol.*, 1968, 22: 131–150.